Design and Analysis of Waveguide-Coupled Photonic THz Transmitters with an Extremely Wide Fractional Bandwidth

Nan-Wei Chen[1], Jhih-Min Wun[2], Hao-Chen Wang[1], Rui-Lin Chao[2,3], Chris Koh[4], C. H. Dreyfus[4] and Jin-Wei Shi[2*], *Senior Member IEEE*

***Abstract*—The design and analysis of novel waveguide-coupled photonic transmitters, which can have an extremely wide ±3-dB fractional optical-to-electrical (O-E) bandwidth at near the THz operating frequency regime (100%; 0.1-0.3 THz), is presented. This novel module is composed of a customized WR-10 based wideband antenna and an ultra-fast/high-power photodiode with a 0.33 THz 3-dB O-E bandwidth, which is flip-chip bonded onto an aluminum nitride (AlN) substrate, integrated with an impedance matching circuit as well as a bow-tie radiator to serve as the antenna feed. The WR-10 based dual-ridge horn structure is adopted to realize the extremely wideband antenna because the dominant TEM mode supported by the dual ridges has no cutoff frequency. The proposed antenna exhibits an over 18 dB gain across the whole operating bandwidth (0.1-0.3 THz). With the transmitter operating at an output photocurrent of 10 mA and employing the same dual ridge-horn antenna at the receiving end, we can detect a reasonable power (31.6 μW) at 0.24 THz through 1 cm wireless transmission.**

***Index Terms*—photodiodes, high-power photodiodes, radio frequency photonics**

I. INTRODUCTION

The application of photonic technology for a fifth generation (5G) millimeter-wave (MMW) wireless communication system is very attractive. In the 5G access fronthaul [1] we can generate optical MMW and data signals in the central office and then transmit them to an antenna in the cell site cabin through low-loss optical fibers. Compared with traditional MMW systems based on metallic waveguides or coaxial cables, the photonic approaches with optical fibers for MMW signal transmission have much lower loss/dispersion and a nearly infinite bandwidth. Due to these advantages, the photonic MMW solution can also greatly enhance the performance in terms of the operating bandwidth, size of the system, phase noise, and complexity of the generated waveform over other traditional MMW or THz systems, including THz communication systems [2], sub-THz/THz vector network analyzers (VNA) [3,4] and chirped pulse radar systems [5]. In the case of photonic VNA for example, it can produce a single sweep of the operating frequency from near dc to THz regime by using just a single photodiode combined with an optical MMW source [6] instead of using different frequency multipliers at different MMW bands with different waveguide and calibration processes [7]. This can lead to great savings of time and cost during THz measurement. The ultrafast and high-power photodiodes (PDs) play important roles in these photonic MMW systems, often determining their maximum available bandwidth, power, and dynamic range [3,8].

An effective solution for photonic sub-THz/THz applications involving the integration of the ultra-fast uni-traveling carrier photodiodes (UTC-PDs) with metallic waveguides was presented in [9,10]. They demonstrated excellent power/bandwidth performances and are now commercially available[1]. Although the antenna-integrated photomixer module [10-12] may have a broader bandwidth than the waveguide-coupled ones, the waveguide package is still preferable for system integration due to the fact that most of the active/passive MMW components, such as amplifiers, horn antennas, and mixers, have waveguide-based input/output ports. Nevertheless, the bandwidths of waveguide-coupled photomixers are usually limited by the intrinsic bandwidth of the metallic waveguides, and their output power is usually around 5-10 dB lower than that of sub-harmonic frequency multiplier modules, which have a very close bandwidth performance and operate at corresponding MMW bands[2].

In this work, we demonstrate a novel waveguide-coupled photonic THz transmitter capable of overcoming the intrinsic bandwidth limitation of the waveguide which can cover most of the low-loss sub-THz windows for wireless transmission (0.1 to 0.3 THz) [13]. The module is mainly composed of a novel ultrafast uni-traveling carrier PD (UTC-PD) with a type-II hybrid absorber [14], dual ridge horn antenna [15], and planar circuits for waveguide/antenna excitation. By using such a transmitter with the same dual ridge horn antenna in the receiving end, we demonstrate the generation, wireless transmission, and detection of THz wave power with an extremely-wide ±3-dB fractional bandwidth (0.1 to 0.3 THz; 100%). Under a 10 mA output photocurrent, we detect an output power of 31.6 μW at 0.24 THz at the receiving-end.

II. TRANSMITTER DESIGN AND CHARACTERIZATION

Figure 1(a) shows the CAD layout for full-wave simulation of the proposed transmitter chip. It is shown that the active PD chip is flip-chip bonded onto a 150-μm thick AlN carrier, where planar passive slotline circuits and a bowtie-shaped waveguide feed are imprinted. The PD-integrated transmitter chip is partially inserted into a WR-6 waveguide with the aid of two alignment grooves on the slotline, and the photo-generated output power from the PD is delivered to the bow-tie radiator

Nan-Wei Chen is with the [1]Department of Communications Engineering, Yuan Ze University, Jhongli, 320, Taiwan. Jhih-Min Wun, and Jin-Wei Shi are with the [2]Department of Electrical Engineering, National Central University, Taoyuan, 320, Taiwan. Rui-Lin Chao is with the [3]Department of Photonics, National Chiao-Tung University, Hsinchu 300, Taiwan. (*email:jwshi@ee.ncu.edu.tw). Chris Koh and C. H. Dreyfus are with the [4]Millimeter Wave Systems LLC, 9 Research Drive STE 8, Amherst, MA, 01002, USA

[1]NTT Electronics Corporation (https://www.ntt-electronics.com/en/products/photonics/utc-pd.html). New Stage YOKOHAMA, 1-1-32 Shin-urashimacho, Kanagawa-ku, Yokohama-shi, Kanagawa, 221-0031, Japan.

[2]Virginia Diodes, Inc., 979 Second Street, S.E. Suite 309, Charlottesville, VA 22902-6172.

This article has been accepted for publication in a future issue of this journal, but has not been fully edited. Content may change prior to final publication. Citation information: DOI 10.1109/JLT.2018.2808932, Journal of Lightwave Technology

for waveguide excitation, as shown in the configuration in Figure 1(b). The entire transmitter module, as depicted in Figure 2, is realized by connecting the WR-6 to a WR-10 based dual ridge horn antenna through a WR-6 to WR-10 waveguide transition. From the microwave network point of view, the entire module is represented as a three-port network, including a photo-generated source input and a 50-Ω matched load as indicated on Fig. 1(b) and the horn opening marked on Fig. 2. The corresponding reflection coefficient, S_{11}, and the transmission coefficient, viz. S_{31}, are extracted at every single frequency of the operating band by means of a co-simulation with the finite-element based full-wave solver, ANSYS HFSS [16], and the high-frequency circuit solver, Keysight ADS [17]. The readers are referred to our previous work [18, 19] for details of the device modeling and system characterization.

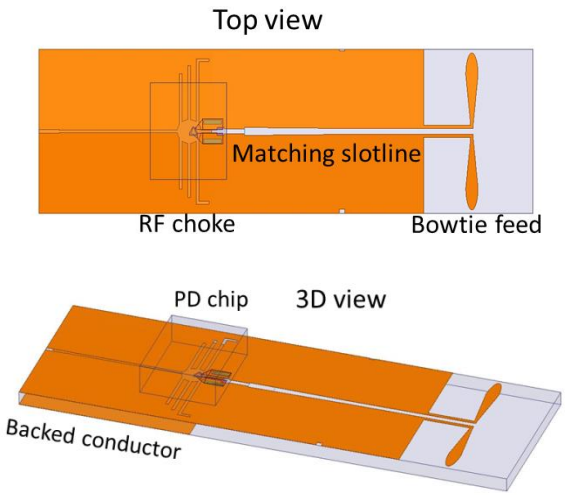

Figure 1. (a) CAD layout of the transmitter chip in our proposed waveguide-coupled photonic transmitter; (b) CAD layout of the feed configuration for the WR-6 waveguide.

The design approach of the transmitter module is essentially similar to that presented in [18], but the upper bound of the operating regime is greatly extended (~300 GHz) thanks to the adopted dual-ridge horn antenna. The planar passive elements used for transmitter chip development, including the notch filter (RF choke), bowtie feed, and tapered slotline between the integrated PD and the feed, are first described below. The design of the dual-ridge horn along with its effect as a load to the transmitted chip is then presented. As shown in Figure 1(a), the RF choke is right below the filp-chip bonded PD chip. With the RF choke, the partially reflected photo-generated source from the bowtie feed is isolated from the PD bias, i.e. a notch filter to block transmission of the photo-generated source. This notch filter is synthesized with slotline short stubs [20-22]. Each of the short stubs introduces a specified transmission zero for realizing the stopband of the photo-generated source; the location and bandwidth of each zero can be independently adjusted with the stub length and the stub characteristic impedance. On the other hand, the PD chip on top of the stubs has a minor impact on the filter performance and is included in the full-wave characterization for filter optimization. In order to ensure wide band operation at the THz regime, some have designed planar circuits with novel topologies for broadening their resonant frequencies [23-25]. Here, for the WR-6 feed in our transmitter, we employ a bowtie-shape dipole structure, a variant of the conventional narrow-band dipole adopted in a previous design [19], for broadband excitation based on the same concept. The broadband nature of the adopted structure is described below.

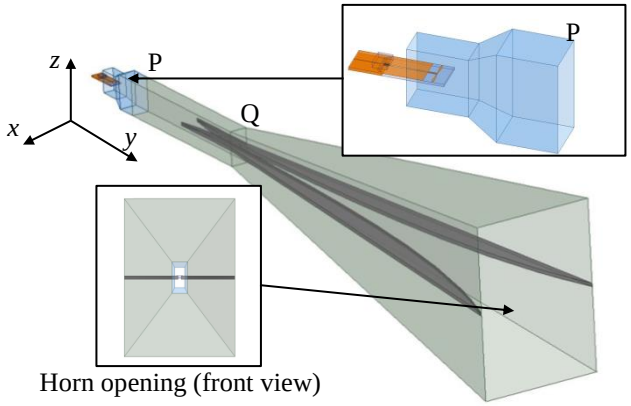

Figure 2. CAD layout of the entire waveguide-coupled photonic transmitter module, including a dual ridge horn antenna.

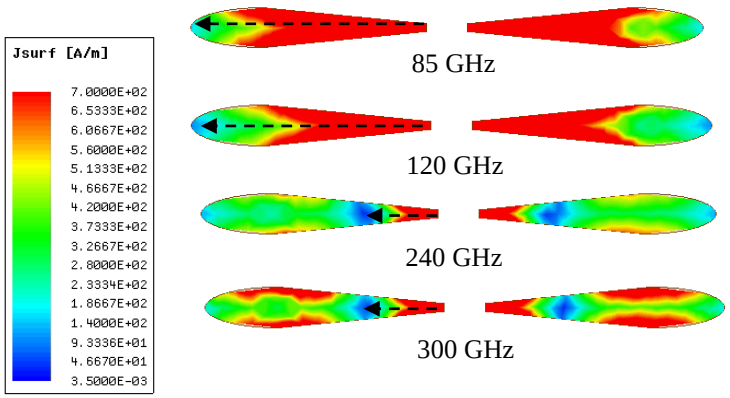

Figure 3. Distribution of the surface current density on the bowtie at different operating frequencies.

The conventional half-wavelength dipole can be categorized as a resonant type antenna, where the wire-shaped structure resonates when the dipole length is near an odd integer times half the wavelength. As all resonances are well separated, a half-wavelength dipole is often employed to operate at its lowest resonant frequency (first resonance) and has a very narrow operating bandwidth. In contrast, the adopted bowtie-

shaped dipole supports the first resonance over a relatively wide range of operating frequencies, since each arm has a linearly tapered body and a rounded end. The distribution of the surface current density on the bowtie at four different operating frequencies is illustrated in Fig. 3. It can be seen that the first-resonance wavelength (four times the length of the dashed arrow), i.e. four times the distance between the current peak (red) and null (blue), decreases sequentially as the frequency increases from 85 to 240 GHz. Furthermore, the onset of the second resonance is observed at 300 GHz. That is, the bowtie can operate at the first resonance from 85 GHz to nearly 300 GHz. Hence, it is suitable for excitation of the fundamental mode of WR-6 over a very wideband. On the other hand, the structure has low insertion loss, as the slotline section between the grooves and the bowtie feed end functions not only as a reflector for the end-fire excitation, but as a reflector for the excited modes. Furthermore, in contrast to a resonant type feed, e.g. the dipole feed, the structure of this sort of device has a relatively mild input-impedance variation over the entire operating band, which results in a simpler matching circuit design, as outlined below. Given the afore-mentioned nature of the feed, a tapered slotline section is capable of attaining a reasonably good match between the PD-integrated notch filter and the feed at the frequencies of interest, and the matching can be mainly optimized with the line length.

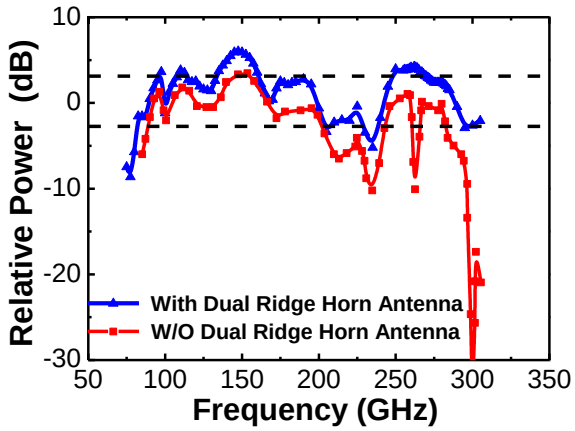

Figure 4. The simulated frequency response of a transfer function for our photonic transmitter without (red trace)/with (blue trace) the dual ridge horn antenna.

The red line in Figure 4 corresponds to the full-wave simulated S_{31}, i.e. the transfer function, of the transmitter module without the transmitting dual-ridge horn antenna. We can clearly see that, by choosing a simulation power of 0.2 THz as a reference point, the ±3-dB bandwidth can cover from 0.1 to 0.29 THz, except for two nulls at around 0.23 and 0. 26 THz. The existence of the null is explained as follows. According to waveguide theory [20], the higher order modes of the WR-6 waveguide start propagating when the operating frequency is over 180 GHz. Hence, the electric field (E-field) pattern at the overmoded waveguide opening starts to deviate from the fundamental TE_{10} mode. For illustration, Figure 5(a) demonstrates the E-field pattern on the waveguide cross section at point P (marked on Figure 2) at 150 GHz. As the frequency is below the cutoff frequency of the first higher order mode, there is only one mode (TE_{10}) excited in the waveguide, which results in a large output voltage (high S_{31}), between the two side walls are normal to the *x* axis. In contrast, examine the E-field pattern for the same cross section at 262.5 GHz (the second null of S_{31}), which is presented in Figure 5(b). Owing to the overmoded operation, the dominant E-field peaks in the upper and lower territories and points in the +*z* direction, which leads to a significant drop in the output voltage (low S_{31}). It can be concluded from this that the relatively low S_{31} at frequencies over 180 GHz is attributable to the overmoded operation. Here, the deterioration in the transfer function can be drastically alleviated with the addition of the proposed dual-ridge horn antenna. Figure 5(c) shows the E-field pattern at the antenna cross section (point Q) at 262.5 GHz for comparison against the one shown in Fig. 5 (b). In contrast to the overmoded field pattern, the cut-off free TEM mode is observed at point Q, thanks to the dual-conductor topology. Indeed, the *x*-directed E-field can be extracted from the overmoded waveguide with two metallic ridges, so the output voltage is greatly enhanced. Below, the dual-ridge horn design followed by full-wave characterization is presented.

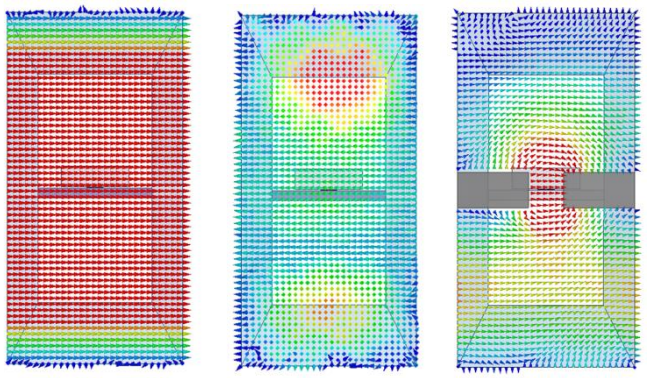

Figure 5. The simulated E-field patterns for: (a) plane P at 150 GHz; (b) plane P at 262.5 GHz; and (c) plane Q at 262.5 GHz.

As depicted in Figure 2, each of the two side walls normal to the *x* axis has a protruding metal blade centered in the middle. The exponentially profiled blade is poised for travelling-wave propagation. Up to 300 GHz, the simulated S_{11} of the antenna (Figure 6 (a)) is less than -20 dB, and the simulated gain (Figure 6(b)) is greater than 25 dB. Figure 7 shows the directional, end-fire patterns at the *xy*-plane for the frequencies at 105, 205, and 305 GHz. The resulting full-wave simulated S_{31} for this directional, broadband transmitting antenna is indicated by the blue line in Figure 4. The resultant S_{31} at frequencies over 180 GHz is significantly improved, and the ± 3-dB bandwidth referenced to 0.2 THz ranges from 0.1 to 0.3 THz. The results of experimental verification of the proposed transmitter module for point-to-point wireless transmission are presented below. The experimental setup is described first, followed by a presentation of the measurement results along with a discussion in Section III.

This article has been accepted for publication in a future issue of this journal, but has not been fully edited. Content may change prior to final publication. Citation information: DOI 10.1109/JLT.2018.2808932, Journal of Lightwave Technology

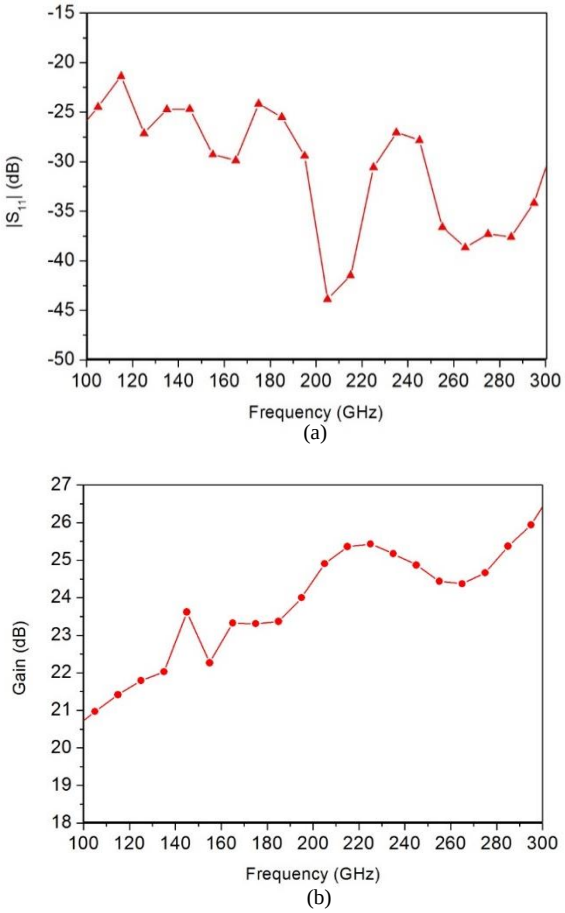

Figure 6. (a) The simulated return loss for the proposed transmitter; (b) the simulated gain for the proposed transmitter.

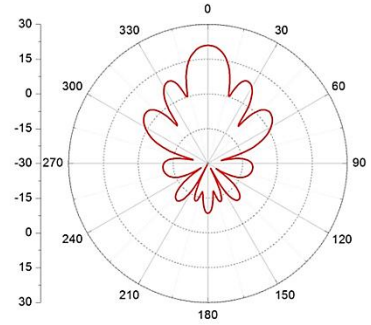

105 GHz

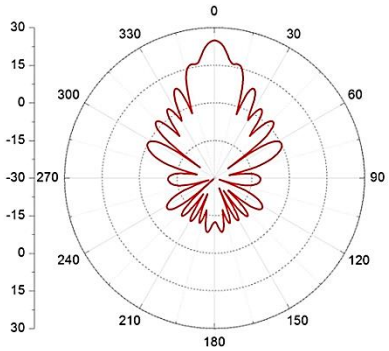

205 GHz

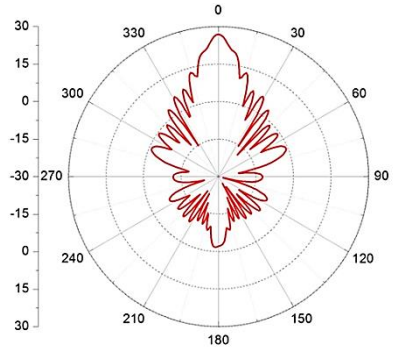

305 GHz

Figure 7. The simulated *xy*-plane gain patterns for the transmitter at 105, 205, and 305 GHz (from top to bottom).

Figure 8(a) shows the top view of the fabricated passive circuits together with the bowtie feed on the AlN substrate, as well as the top view of the PD chip. The top view of the entire transmitter chip after flip-chip bonding of the PD onto the substrate is presented in Figure 8(b). The micro-machined dual-ridge horn antenna is shown on the right of Figure 9, and the point-to-point wireless transmission setup is presented on the left of Figure 9. As shown in Figure 9, a WR-10 based dual-ridge horn is employed as the transmitting/receiving antenna, and the horn is connected to the WR-6 feed via a tapered waveguide. At the receiving end, the received power is measured with a thermal power meter (PM4, VDI-Erickson[1]). The distance between two horn openings is 1 cm.

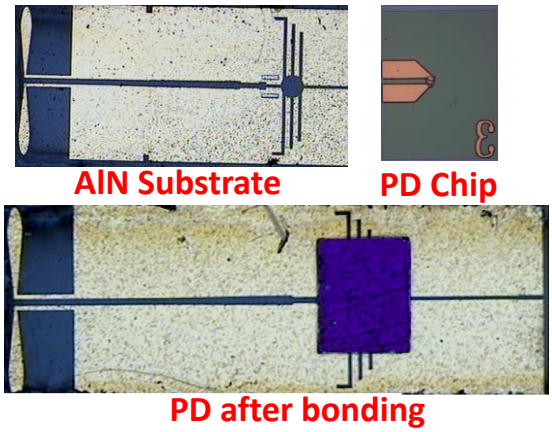

Figure 8. Top-view of the fabricated photonic transmitter chip: (a) before; and (b) after flip-chip bonding.

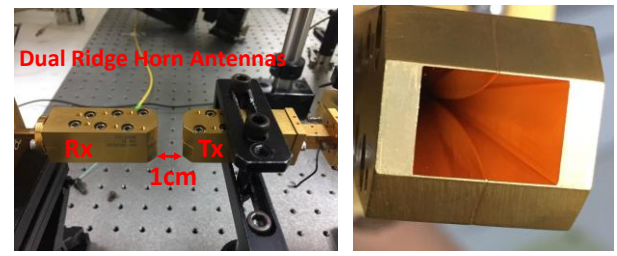

Figure 9. Photo of the wireless transmission setup and the fabricated dual ridge horn antenna.

This article has been accepted for publication in a future issue of this journal, but has not been fully edited. Content may change prior to final publication. Citation information: DOI 10.1109/JLT.2018.2808932, Journal of Lightwave Technology

III. Measurement Results and Discussion

A typical two-laser heterodyne beating system is adopted in our setup to test the O-E frequency responses and photo-generated THz power from our transmitter [26]. During measurement, the output photo-generated electrical power from the PD should include the component of the difference frequency between the two lasers used in this setup, due to fact that the PD (photomixer) is intrinsically a nonlinear device. Its output photocurrent (I) is linearly proportional to the input optical power, which leads to a square relation between the input optical power vs. the output electrical power from the PD ($I^2 \times R$; where R is the load resistance of PD). Figures 10 (a) and (b) show the measured O-E frequency response of our PD with active diameters of 3 and 5 μm active, respectively, after flip-chip bonding and under a load of 50 Ω [14]. We can clearly see that for the 3 μm device, under an output photocurrent of 5 mA and an optimum bias of -0.5 V, the measured maximum 3-dB O-E bandwidth can reach 0.33 THz, which meets the bandwidth required for photonic transmitter, as discussed latter. On the other hand, there is a degradation of the 3-dB O-E bandwidth of 5 μm device to 150 GHz due to the decrease in the RC-limited bandwidth [14].

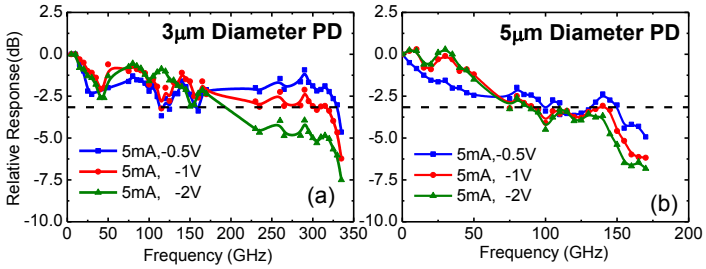

Figure 10. (a) The measured O-E frequency responses of our active PD with: (a) 3; and (b) 5 μm active diameters.

Figure 11 (a) shows the measured frequency response of the fully wireless transmitter module at the receiving end. The output photocurrent is fixed at 8 mA during the measurement. Here, the black and green traces represent the measured traces from two different modules (Transmitter 1 and 2) but with the same package and same PD active diameter of 3 μm. We can clearly see that both modules have very similar O-E frequency responses and can cover the 0.1 to 0.3 THz operating frequency. Choosing the detected power at 0.2 THz as a reference point, the measured ± 3-dB optical-to-electrical (O-E) bandwidth can be as wide as 0.2 THz (0.1 to 0.3 THz). This corresponds to a 100% fractional bandwidth. The fractional bandwidth achieved here should be the highest reported among waveguide-coupled photonic transmitters [9,10]. Figure 11 (b) shows the measured frequency response for the same transmitter module but with 3 and 5 μm active diameter PDs packaged inside. As can be seen, under the same output photocurrent (8 mA), the transmitter module with a 3 μm PD exhibits a much better O-E bandwidth than does the 5 μm device due to its much wider O-E bandwidth performance (0.33 vs. 0.15 THz), as discussed above.

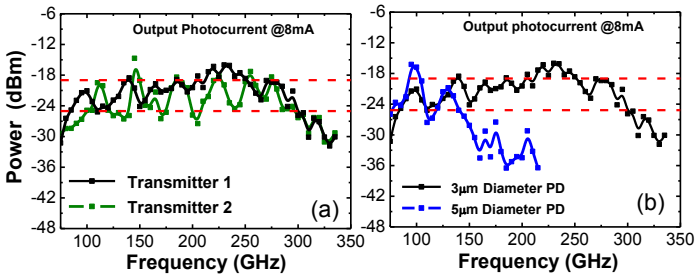

Figure 11. The measured O-E frequency responses of our wireless transmission channel (photonic transmitter with receiving antenna) with: (a) 3 μm; and (b) 5 μm active diameter PDs packaged into the transmitter module

The gain, *G*, of the adopted dual-ridge horn antenna at these operating frequencies can be extracted using the same measurement setup and calculated with the Friss transmission formula shown below.

$$P_r = P_t + 2G + 20\log_{10}(\frac{\lambda}{4\pi r}), \quad (1)$$

where P_t is the photo-generated THz power fed into the dual ridge horn antenna, P_r is the available power at the receiving antenna terminal, λ is the free-space wavelength, and r is the distance between the phase centers of the transmitting and receiving antennas, which is a function of the λ and can be determined with the far-zone radiation fields [27]. More specifically, the far-zone fields are calculated with a given aperture field distribution at the horn opening. Here, the TEM mode supported by the two ridges is assumed in the field calculations. The resulting phase center location, termed *d* in [27], is first extracted and approximated as d ≈ 14λ. With the geometrical parameters of the horn as defined in [27], $r_z = 50$ mm and $\alpha_0 = 7.3°$, the distance between the horn aperture and the phase center is then obtained with $r_z \cos\alpha_0 - d$. The r in eq. (1) is simply equal to the sum of the separation between the two horn apertures, i.e. 1 cm, and 2($r_z \cos\alpha_0 - d$). Table 1 shows the extracted gains at different operating frequencies, which agree well with the simulated results shown in Figure 6(b). The slight discrepancy between the tabulated results and the ones shown in Figure 6(b) might be attributed to the deviation of the actual aperture fields from the assumed ones (TEM mode). More specifically, the existence of closed metallic walls leads to a relatively large field inconsistency at lower frequencies, whereas the fields at higher frequencies tend to be confined in the vicinity of the ridge gap and more closely resemble the assumed TEM mode.

To demonstrate the performance of the proposed waveguide coupled photomixer, the measured O-E frequency responses, in terms of bandwidth and power, are compared against the ones obtained with a commercially available photomixer. Figure 12 shows the measured O-E frequency responses for our home-made transmitter module (3 μm PD inside) and for the commercially available W-band photomixer[1] (IOD-PMW-13001) measured under the same test setup, as shown in Figure 9, and the same output photocurrent of 8 mA. We can clearly see that our home-made device has a broader fractional

[1]NTT Electronics Corporation (https://www.ntt-electronics.com/en/products/photonics/utc-pd.html). New Stage YOKOHAMA, 1-1-32 Shin-urashimacho, Kanagawa-ku, Yokohama-shi, Kanagawa, 221-0031, Japan.

This article has been accepted for publication in a future issue of this journal, but has not been fully edited. Content may change prior to final publication. Citation information: DOI 10.1109/JLT.2018.2808932, Journal of Lightwave Technology

bandwidth and can attain a higher output power than those of the commercial photomixer when the operating frequency is over 160 GHz. The measurement results reflect the trade-off between output power and fractional bandwidth in the design of waveguide-coupled photomixer.

TABLE I. EXTRACTED GAIN OF DUAL RIDGE HORN ANTENNA AT DIFFERENT OPERATING FREQUENCIES

f (GHz)/λ (mm)	P_t (dBm)	P_r (dBm)	G (dB)
100/3.0	-29	-24.63	18.2
145/2.07	-23.9	-18.64	21.4
180/1.67	-24.36	-19.55	24.4
200/1.5	-24.45	-17.55	24.1
265/1.13	-25.53	-19.17	26.2

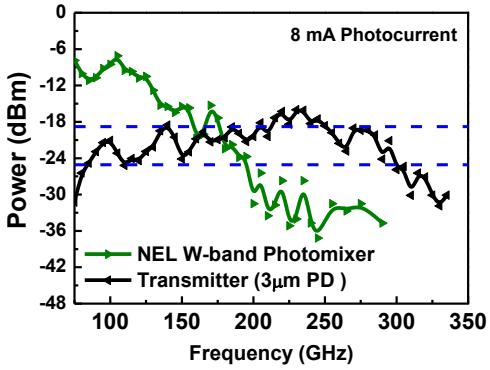

Figure 12. The measured O-E frequency responses for our wireless transmission channel (photonic transmitter with receiving antenna) design obtained using our home-made transmitter (black trace) and the commercial one (green trace).

Figures 13 (a) and (b) show a comparison between the simulated and measured frequency responses of our transmitter module, with and without the dual ridge horn antenna, respectively. For the case without the antenna, a power meter with an WR-10 input is employed to replace the dual ridge horn antenna for received power measurement. Again, the high power fluctuation at the higher frequencies for the case without the dual-ridge horn can be attributed to the afore-demonstrated overmoded operations. The disagreement between the simulated and measured results is addressed as follows. The relatively large discrepancy observed in both figures at the frequencies from 80 to 230 GHz is attributed to the surface leaky wave excited in the conductor-backed slotline-see Figure 7 in [28]. In the measurement, the evanescent leaky wave is excited and leads to a higher power loss as well as a variation on the characteristic impedance. In contrast, surface wave of this sort is not observed in the simulation owing to the delta-gap source (TEM mode excitation) [29] for modeling the photo-generated source input in Fig. 1(b).

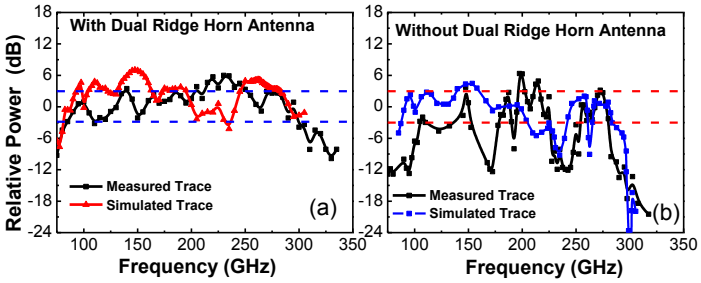

Figure 13. The measured and simulated O-E frequency responses for our photonic transmitter module: (a) with; and (b) without the dual ridge horn antenna.

Figure 14 shows the power measured at the receiving end versus the output photocurrent on the transmitter side. The operating frequency is fixed at 0.24 THz. The red line is the ideal photo-generated THz power versus photocurrent for a 100% optical modulation depth and a 50-Ω load. The difference between the measured power and the ideal curve represents the summation of 4 dB loss from the non-ideal (~63 %) optical modulation depth in our hetero-dyne beating system [14], radiation loss, and waveguide coupling loss for our setup. We can clearly see that all three tested devices (Tx 1 to Tx 3) showed a close value of maximum detected power at around 31.6 μW with the same saturation current at around 10 mA. A higher receiving power can be expected by installing a Teflon based THz lens to focus the power emitted from transmitting antenna onto the receiving one to minimize the radiation loss [10-12]. Compared to the saturation current reported for a PD with the same active diameter but a different package [14], the measured saturation current here is smaller (10 vs. 13 mA). As shown in Figure 1, this result can be attributed to fact that our active PD is flip-chip bonded onto a narrow AlN stripe for insertion into the WR-6 waveguide, which is suspended in air and has poorer heat sinking than that of a PD flip-chip bonded onto a large area (~1mm^2) AlN carrier [14].

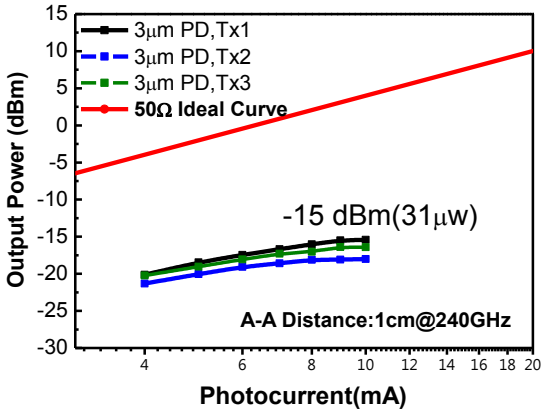

Figure 14. The detected power at the receiving-end at 0.24 THz versus output photocurrent from our photonic transmitters. Tx 1 to Tx 3 represent the three different photonic transmitters with the same packaging, same active PD inside, and under the same test setup.

IV. CONCLUSION

In conclusion, we have demonstrated a novel waveguide-coupled photonic transmitter. By use of a dual ridge horn design for the antenna and a planar circuit for waveguide excitation, the higher-order mode in the WR-6 waveguide can be suppressed. This transmitter achieves an extremely wide fractional bandwidth of 100% (0.1 to 0.3 THz) with high detected power at the receiving-end (31.6 μW) at 0.24 THz through wireless transmission.

V. ACKNOWLEDGEMENT

This project was sponsored by the Ministry of Science and Technology in Taiwan under grant number 105-2622-E-008-014-CC2 and the Asian Office of Aerospace Research and Development (AOARD) under grant number FA2386-17-1-0033.

REFERENCES

[1] S. E. Alavi, M. R. K. Soltanian, I. S. Amiri, M. Khalily, A. S. M. Supa'at and H. Ahmad, "Towards 5G: A Photonic Based Millimeter Wave Signal Generation for Applying in 5G Access Fronthaul," *Scientific Reports*, vol. 6, pp. 19891, Jan., 2016.

[2] S. Koenig, D. Lopez-Diaz, J. Antes, F. Boes, R. Hennberger, A. Leuther, A. Tessmann, R. Schmogrow, D. Hillerkuss, R. Palmer, T. Zwick, C.Koss, W. Freude, O. Ambacher, J. Leuthold, and I. Kallfass, "Wireless sub-THz communication system with high data rate ," *Nature Photonics*, vol. 7, pp. 977-981, Dec., 2013.

[3] T. Nagatsuma, M. Shinagawa, N. Sahri, A. Sasaki, Y. Royter, and A. Hirata, "1.55- m Photonic Systems for Microwave and Millimeter-Wave Measurement," *IEEE Trans. Microwave Theory Tech.*, vol. 49, pp. 1831-1839, Oct., 2001.

[4] S. Preu, "Components Towards a Photonics Aided THz Vector Network Analyzer," *Proc. OFC 2016, Anaheim*, CA, USA, March, 2016, pp. W4K.4.

[5] Y. Li, A. Rashidinejad, J.-M. Wun, D. E. Leaird, J.-W. Shi, and A. M. Weiner, "Photonic Generation of W-band Arbitrary Waveforms with High Time-Bandwidth Products Enabling 3.9mm Range Resolution," *Optica* vol. 1, no. 6, pp. 446-454, Dec., 2014.

[6] A. Hallal, S. Bouhier, and F. Bondu, "Synthesis of a 30-Hz Linewidth Wave Tunable Over 500 GHz," *IEEE Trans. Microwave Theory Tech.*, vol. 65, pp. 1367-1371, April, 2017.

[7] Z. Popović and E. N. Grossman, "THz Metrology and Instrumentation," *IEEE Trans. Terahertz Science Tech.*, vol. 1, pp. 133-144, Sep., 2011.

[8] J.-M. Wun, H.-Y. Liu, Y.-L. Zeng, S.-D. Yang, C.-L. Pan, C.-B. Huang, and J.-W. Shi, "Photonic High-Power CW THz-Wave Generation by Using Flip-Chip Packaged Uni-Traveling Carrier Photodiode and Femtosecond Optical Pulse Generator," *IEEE/OSA Journal of Lightwave Technology*, vol. 34, pp. 1387-1397, Feb., 2016.

[9] A. Wakatsuki, T. Furuta, Y. Muramoto, T. Yoshimatsu, and H. Ito, "High-power and Broadband Sub-terahertz Wave Generation Using a J-band Photomixer Module with Rectangular-waveguide Output Port," *Tech. Dig. 2008 Infrared, Millimeter and Terahertz Waves (IRMMW-THz 2008)*, pp. M4K2 1199, Sep., 2008.

[10]T. Ishibashi, Y. Muramoto, T. Yoshimatsu, and H. Ito, "Unitraveling-Carrier Photodiodes for Terahertz Applications," *IEEE J. of Sel. Topics in Quantum Electronics*, vol. 20, pp. 3804210, Nov./Dec., 2014.

[11] C. C. Renaud, M. Natrella, C. Graham, J. Seddon, F. V. Dijk, and A. J. Seeds "Antenna Integrated THz Uni-Traveling Carrier Photodiodes," *IEEE J. of Sel. Topics in Quantum Electronics*, vol. 24, No. 2, pp. 8500111, March,/April, 2018.

[12] H. Ito and T. Ishibashi, "Photonic Terahertz-Wave Generation Using Slot-Antenna-Integrated Uni-Traveling-Carrier Photodiodes," *IEEE J. of Sel. Topics in Quantum Electronics*, vol. 23, pp. 3800907, July/August, 2017.

[13] J. Wells, "Faster Than Fiber: The Future of Multi-Gb/s Wireless," *IEEE Microwave Magazine.* vol. 10, pp. 104-112, May, 2009.

[14]J.-M. Wun, Y.-W. Wang, and J.-W. Shi, "Ultra-Fast Uni-Traveling Carrier Photodiodes with $GaAs_{0.5}Sb_{0.5}/In_{0.53}Ga_{0.47}As$ Type-II Hybrid Absorbers for High-Power Operation at THz Frequencies," *IEEE J. of Sel. Topics in Quantum Electronics*, vol. 24, No. 2, pp. 8500207, March,/April, 2018.

[15] V. Rodriguez, "The dual-ridged horn antenna," *EE, Evaluation engineering* vol. 45, No. 10, pp. 58-63, Oct., 2006.

[16] ANSYS HFSS:3D full-wave electromagnetic field simulation, ANSYS, Inc.

[17] Keysight ADS, Keysight Technologies, 1400 Fountaingrove Parkway, Santa Rosa, CA 95403-1799.

[18] N.-W. Chen, H.-J. Tsai, F.-M. Kuo, and J.-W. Shi, "High-Speed W-Band Integrated Photonic Transmitter for Radio-Over-Fiber Applications," *IEEE Trans. Microwave Theory Tech.*, vol. 59, No. 4, pp. 978-986, April, 2011.

[19] N.-W. Chen, J.-W. Shi, F.-M. Kuo, J. Hesler, T. W. Crowe, and J. E. Bowers, "25 Gbits/sec Error-Free Wireless Link between Ultra-Fast W-Band Photonic Transmitter-Mixer and Envelop Detector," *Optics Express*, vol. 20, No. 19, pp. 21223-21234, Sep., 2012.

[20] D. M. Pozar, *Microwave Engineering*, 4th ed. New York: Wiley, 2011.

[21] K.C. Gupta, R. Garg, I. Bahl,R.Bhartia, *MicrostripLines and Slotlines*, Artech House, Inc., Norwood, MA, 1996.

[22] G. Mattaei, L. Young, and E. M. T. Jones, *Microwave filters, impedance matching networks, and coupling structures*, Artech House, Norwood, MA, 1980.

[23] Y. Peng, X.-F. Zang, Y.-M. Zhu, C. Shi, L. Chen, B. Cai, and S.-L. Zhuang, "Ultra-broadband terahertz perfect absorber by exciting multi-order diffractions in a doublelayered grating structure," *Optics Express*, vol. 23, No. 03, pp. 2032-2039, Feb., 2015.

[24] X.- F. Zang, C. Shi, L. Chen, B. Cai, Y.-M. Zhu, and S.-L. Zhuang, "Ultra-broadband terahertz absorption by exciting the orthogonal diffraction in dumbbell-shaped gratings," *Scientific Reports*, vol. 5, pp. 8901, March, 2015.

[25] C. Shi, X.-F. Zang, L. Chen, Y. Peng, B. Cai, G. R. Nash, and Y.-M. Zhu, "Compact Broadband Terahertz Perfect Absorber Based on Multi-Interference and Diffraction Effects," *IEEE Trans. Terahertz Science Tech.*, vol. 6, pp. 40-44, Jan., 2016.

[26] S. Kawanishi, and M. Saruwatari, "A Very Wide-Band Frequency Response Measurement System Using Optical Heterodyne Detection," *IEEE Trans. Instrumentation and Measurement*, vol. 38, pp. 569-573, April, 1989.

[27] Y.-Y. Hu, "A Method of Determining Phase Centers and Its Applications to Electromagnetic Horns," *Journal of the Franklin Institute*, vol. 271, pp. 31–39, Jan. 1961.

[28] J. Zehentner, J. Machac, and J. Mrkvica, "Modes on standard and inverted conductor-backed slotline," 2003 *IEEE IMS* Symposium, June 8-13, pp.1-4.

[29] R. King and D. D. King, "Microwave Impedance Measurements with Application to Antennas .II," *Journal of Applied Physics*, vol. 16, pp. 445-453, 1945.